Proceedings of the ASME 2024
International Mechanical Engineering Congress and Exposition
IMECE2024
November 17-21, 2024, Portland, Oregon

IMECE2024-145569

HYDRODYNAMICS OF SHRIMP SWIMMING: SPREAD-OUT MORPHING OF PLEOPODS IN POWER STROKE

Zhipeng Lou[1], Nils Tack[2], Monica Wilhelmus[2], Chengyu Li[1]

[1] *Case Western Reserve University, Cleveland, OH 44106, USA*

[2] *Brown University, Providence, RI 02912, USA*

ABSTRACT

Shrimps locomote through water using five pairs of appendages known as pleopods, which beat in a coordinated metachronal motion. Each pleopods consists of two membranous rami, a medial endopod and lateral exopod whose edges are lined with fine hair-like setae. Because of their close spacing and density, the setae act as an impermeable membrane. During swimming, each pleopod executes a power stroke, propelling water backward, followed by a recovery stroke to reset its position. During the power stroke, the exopods, endopods, and setae spread out, forming a propulsor with a larger area. In contrast, the rami close and overlap during the recovery stroke, reducing the effective area. In this study, we simulate natural shrimp swimming based on high-speed recordings under Reynolds number (Re) of 1980, using an in-house computational fluid dynamics (CFD) solver. We compared a model based on a natural swimming shrimp with a model with pleopod area fixed at the maximum area. Our results reveal that the model incorporating spread-out motion achieves a notable reduction of 49.84% in cycle-averaged hydrodynamic power while sacrificing only 23% of cycle-averaged thrust when compared to the fixed-pleopod area model. Furthermore, the effect of spread-out motion decreases the cost of transportation by 41.72% through reducing body drag by 12%. Additionally, our analysis observed the presence of a high-speed zone behind the second pleopod during stroke motion, particularly near the tangent plane of the lowest tip trajectory, and a low-speed zone in front of that pleopods.

NOMENCLATURE

$\bar{U}_{tip}$	Mean pleopod tip speed
U_∞	Swimming speed
u_i	Velocity component
L_p	Pleopod length
L_b	Body length
W	Body weight
f	Stroke frequency
T	Cycle period
p	Pressure
ν	Fluid kinematic viscosity
ρ	Fluid density
Re	Reynolds number
Re_w	Oscillatory Reynold number
St	Strouhal number
J	Advance ratio
COT	Cost of transport
Ta	Temporal asymmetry parameter

1. INTRODUCTION

Marsh grass shrimps (*Palaemonetes vulgaris*) employ metachronal paddling, a widely adopted locomotory strategy known for its efficiency among animals equipped with multiple swimming appendages[1–4]. During metachronal paddling,

propulsion is generated as appendages stroke against the swimming direction one after another, with certain phase lag.The first phase of a beat, the power stroke, is responsible for propulsive thrust. Following a power stroke, the appendages return to their initial position through the recovery stroke, encountering drag force [5–10]. Enhancing metachronal swimming efficiency involves either increasing thrust output during power strokes or reducing drag during recovery strokes.

Evidence suggests that power strokes rely on suction force from a negative pressure zone in front of appendages rather than pushing force behind them [9]. Shrimps are believed to leverage flexible pleopods to create a "cup" effect, enhancing suction in front of the pleopods [11]. However, increased thrust may escalate power consumption, potentially compromising propulsive efficiency. Conversely, drag reduction offers a dual benefit of boosting total thrust while reducing power consumption. For instance, copepods' appendages are observed to cohesively group during recovery strokes, reducing drag from multiple appendages to that of a single one [12]. Similarly, ctenophores exhibit drag reduction through appendage interactions that weaken vortex formation [8]. Nevertheless, there exists a strategy evolved by numerous species employing drag-based propulsion, which achieves both: increasing thrust during power strokes and reducing drag during recovery strokes. This integrated approach involves spreading out during the power stroke and collapsing during the recovery stroke. By addressing both aspects within one strategy, the need for separate strategies is eliminated, simplifying engineer designs for practical application.

This spread-and-fold morphing motion are widely observed among vertebrates [13,14] and invertebrates [15–17]. During the power stroke, animals spread out their appendages to increase the surface area, achieved through various mechanisms that vary among species. For example, in krill, the two segments, exopods and endopods, actively separate during power strokes, with the setae lining their edges also fanning out, likely enhancing thrust [17]. In the subsequent recovery stroke, animals fold their appendages back to minimize surface area and drag.

However, few studies have delved into the potential effects on the flow field. Understanding how spread-out morphing increases thrust during the power stroke and how folding-back morphing reduces drag could provide valuable insights. Additionally, it remains unclear whether the thrust gained from morphing motions might lead to excessive power consumption, potentially compromising propulsive efficiency.

This study employs an in-house computation fluid dynamic (CFD) solver to investigate free-swimming shrimp, whose pleopods spread out during the power stroke and fold back during the recovery stroke. Our analysis aims to offer guidance for engineering designs employing spread-and-fold morphing motion.

2. METHODOLOGY

2.1 Kinematics

The swimming of the marsh grass shrimp (*P. vulgaris*) was captured using two cameras: one positioned to capture a side view and another for a back view. The recorded data revealed a swimming speed, denoted as, U_∞, of 0.07 m/s, and a beating frequency f of 6.27. The Strouhal number (*St*), calculated as $St = f\bar{L}_p/U_\infty$, equates to 0.22, with an averaged pleopod length $\bar{L}_p$ of 2.6 mm. This *St* value closely resembles that of the Mantis shrimp, ranging from 0.23 to 0.58 [18] and the Antarctic krill, at 0.38 [3]. Notably, a *St* range of 0.2 to 0.4 indicates efficient locomotion for both flying and swimming organisms, suggesting that the swimming behavior of the shrimp is efficient.

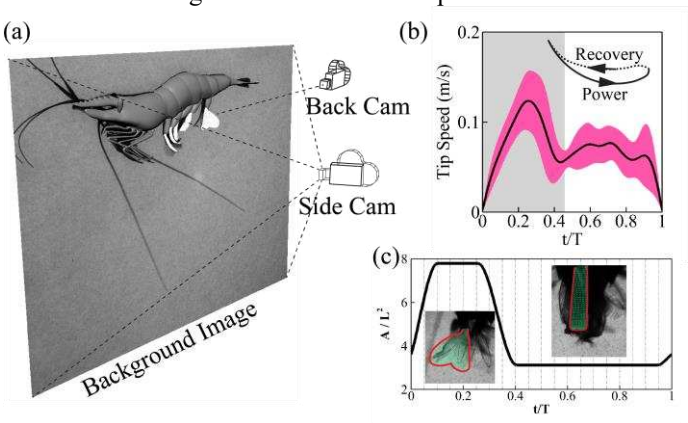

Figure 1. (a) Illustration of reconstructed shrimp model and the background images in Autodesk MAYA. (b) The time history of tip speed and the tip trajectory of the 1st pair of pleopods. The back curve represents the average speed of five pairs of pleopod, and the deviation of them is colored by pink. The shaded area represents the averaged power stroke period.

Autodesk MAYA was used for the reconstruction of the shrimp. In this process, the images captured by the side camera were used as a background reference (see Figure 1a). By aligning the model with these background images, an accurate representation of the real shrimp was achieved. Figure 1b shows the time history of the reconstructed average tip speed and the tip trajectory. The solid line illustrates the trajectory during the power stroke, while the dotted line represents the trajectory during the recovery stroke. Notably, the recovery stroke trajectory differs from that of the power stroke, indicating spatial asymmetrical motion. The average duration of the power stroke across five pleopods (T_p) was recorded at 0.46, shorter than the recovery stroke period (T_r) of 0.54. The temporal asymmetry parameter ($\mathrm{Ta} = (T_r - T_P)/(T_r + T_P)$) is calculated at 0.08 which indicates a small temporal asymmetry, indicating a minor temporal asymmetry compared to other animals [19]. The oscillatory Reynolds number ($Re = 2\pi f {L_p}^2/\nu$) for this shrimp swimming is 253.74. Under such Reynolds number, the Ta of *B. infundibulum*, at around 0.6, exhibits more pronounced asymmetric strokes than those observed in this study [19]. Additionally, the advance ratio ($J = U_\infty / U_{tip}$) is 0.96,

indicating that the swimming speed closely aligns with the tip velocity.

Additionally, the back view camera was employed to reconstruct the morphing motion of the pleopods. Shrimp pleopods consist of exopods and endopods whose edges are lined with fine hair-like setae. During the power stroke, the setae spread out as the exopod abducts. Given the non-permeability of these setae, the pleopods and setae were modeled as a cohesive membrane whose area increases during the power stroke and decreases during the recovery stroke (Figure 1c). The time history of normalized pleopod area is also shown in Figure 1c.

2.2 Governing equations and numerical method for the flow

The governing equations for the shrimp swimming are the unsteady incompressible viscous Navier-Stokes equations, which are shown in equation (1) and (2), and discretized using the collocated grid arrangement, where the primitive variables (u_i and p) are stored in the cell center.

$$\frac{\partial u_i}{\partial x_i} = 0 \tag{1}$$

$$\frac{\partial u_i}{\partial t} + \frac{\partial (u_i u_j)}{\partial x_j} = -\frac{1}{\rho}\frac{\partial p}{\partial x_i} + \nu \frac{\partial}{\partial x_j}\left(\frac{\partial u_i}{\partial x_j}\right) \tag{2}$$

where u_i (for i = 1,2,3) denotes the velocity components in the x, y, and z directions respectively, p is the normalized pressure and Re is the Reynolds number which is defined as $Re = U_\infty L/\nu$.

The above equations are solved by a finite difference-based immersed-boundary method in a non-body-conforming Cartesian grid, which are integrated in time using the fractional step method. The advantage of the immersed-boundary method is that it is not necessary to use complicated re-meshing algorithms that are used by other conventional body conformal methods. Details of the CFD solver used for solving the Navier–Stokes equations are extensively discussed in our previous studies [8,20–22]. This solver has been thoroughly validated for both internal and external fluid flow problems [6,23–25] and has been successfully applied to bio-inspired propulsion studies [26–29].

2.3 Simulation setup

The shrimp was placed at the center of a flow domain measuring $30L_p \times 30\ L_p \times 30\ L_p$, where L_p denoting pleopod length. This domain was discretized into a non-uniform grid comprising 9.97 million nodes. The computational mesh was designed with two layers to balance computational efficiency and mesh quality. As illustrated in in Figure 2a, the denser layer of mesh closely envelops the model, while a second, coarser layer wraps around it to cover the near flow field. The far field is the coarsest, ensuring a smooth transition to the domain boundary. A constant inflow boundary condition was applied to the frontal boundary, while all other boundaries were set to zero-gradient conditions. In all the simulations, the Reynolds number ($Re = U_\infty L/\nu$) is 1980.

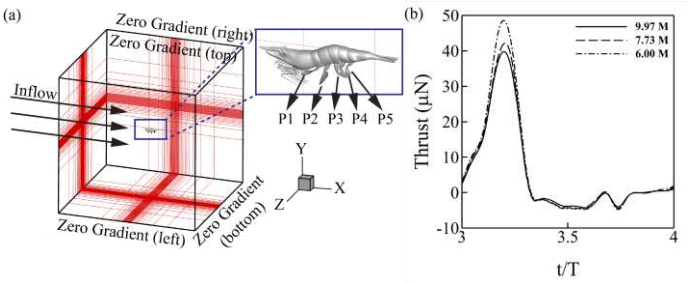

Figure 2. (a) Illustration of the two-layer computational mesh and boundary conditions. (b) Grid independence study through the time history of thrust under grid size of 6.00 million, 7.73 million and 9.97 million.

3. RESULTS AND DISCUSSIONS

This study investigates the impact of spread-out morphing motion of the pleopod by comparing two cases: the baseline case and the fixed-pleopod area (FPA) case. The baseline case represents the natural shrimp with the spread-out morphing motion, while the FPA case involves a model with the pleopod area fixed at its maximum. To ensure stability, four stroke cycles are simulated, and the results presented are based on the fourth cycle.

Using our solver to solve the flow field, wake structures are visualized via iso-surfaces defined by the Q-criterion, as depicted in Figure 3. As a result of the stroke motion, vortices form and detach from the tip, ultimately forming vortex rings in the downwash region. Comparatively, the wake structure in the baseline case is smaller than that in the FPA case, suggesting that the FPA model generates broader range of disturbance in the downwash.

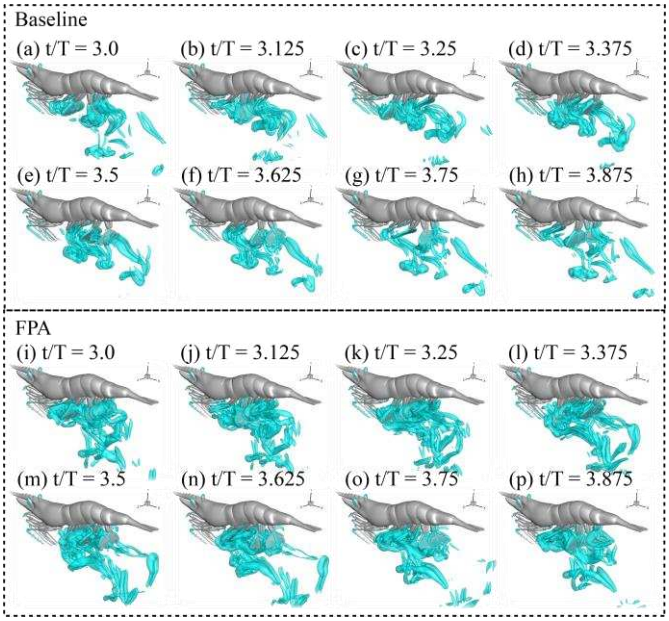

Figure 3. Iso-surface defined by Q-criterion at 8 time instants for (a-h) the baseline case, (i-p) the fixed-pleopod-area (FPA) case.

Figure 4 displays the average time history of mean thrust and hydrodynamic power for five pairs of pleopods, summarizing the collective performance across the fourth period. In the baseline scenario, the thrust remains consistently positive. However, in the FPA case, although thrust generally follows this positive trend, there is a notable exception where it dips below zero around mid-stroke. Furthermore, peak thrust values in the FPA case are typically higher than those observed in the baseline scenario. Similarly, all peak power values recorded in the FPA case surpass those in the baseline case.

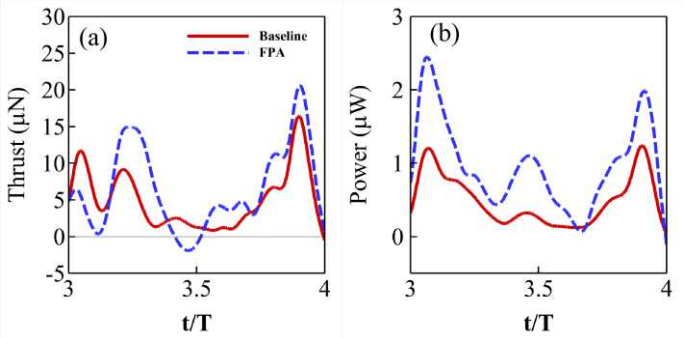

Figure 4. The time history of (a) The mean thrust and (b) the mean hydrodynamic power in the baseline case and FPA case.

Furthermore, for a more comprehensive comparison of the overall performance between the two cases, Figure 5 illustrates the cycle-averaged thrust and power of each pair of pleopods. In the baseline case, the cycle-averaged thrust measures 5.05 μN, marking a 23.01% decrease over the FPA case's 6.57 μN. Additionally, the cycle-averaged power consumption in the baseline case totals 0.49 μW, representing a significant 48.10% drop compared to the FPA case's 0.98 μW. It is noteworthy that the power consumption of the shrimp's body in the baseline case is 1.15 μW, a 12% decrease from the FPA case's 1.29 μW. This disparity suggests that the spread-out morphing motion can mitigate drag on the body, thus reducing energy dissipation.

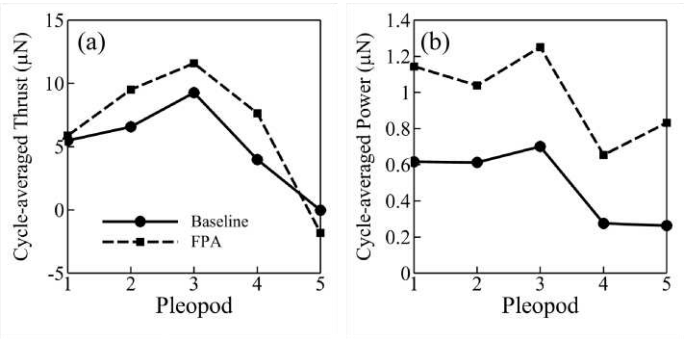

Figure 5. (a) Cycle-averaged thrust and (b) cycle-averaged power for each pair of pleopods.

To assess energy expenditure regardless of swimming velocity and weight, the cost of transport (COT) is calculated as follows: $\mathrm{COT} = \mathrm{power}/(U_\infty \times W)$, where W represents the shrimp weight at 2.04 mN. For the baseline scenario, the COT is 0.024, compared to 0.041 for the FPA scenario. The adoption of spread-out morphing motion results in a reduction of COT from 0.041 to 0.024, representing a decrease of 41.72%.

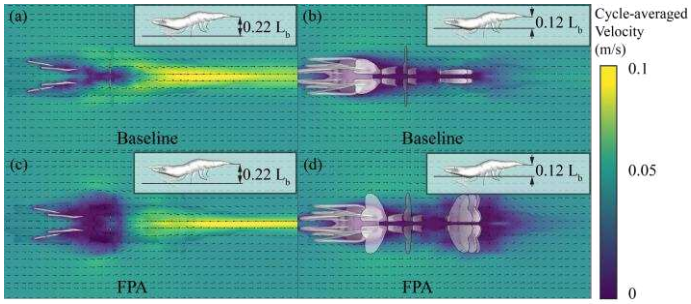

Figure 6. The cycle-averaged velocity field at (a) 0.22 L_b from body and (b) 0.12 L_b from body in baseline case. The cycle-averaged velocity field at (c) 0.22 L_b from body and (d) 0.12 L_b from body in FPA case.

Figure 6 illustrates a comparison of the cycle-averaged velocity field between two cases. In both cases, as shown in Figure 6a and 6c, the velocity closely in front of P2 remains low, exhibiting a low-speed zone. However, a region of higher speed forms along the shrimp centerline behind the second pleopods. The flow velocity in this high-speed zone is notably greater behind P2 compared to that in front of P2. These observations are based on the cross-section contour of the plane positioned 0.22Lb below the telson. To validate the horizontal level of this high-speed zone, the velocity field is also depicted at 0.12Lb below the telson in Figure 6b and 6d, where the high-speed zone is not observed. Hence, this high-speed zone predominantly exists at a lower level, approximately near the tangent plane of the lowest tip trajectory of P2. Furthermore, a comparison between Figure 6a and 6c, or Figure 6c and 6d, indicates that the low-speed zone in the FPA case is wider than in the baseline case.

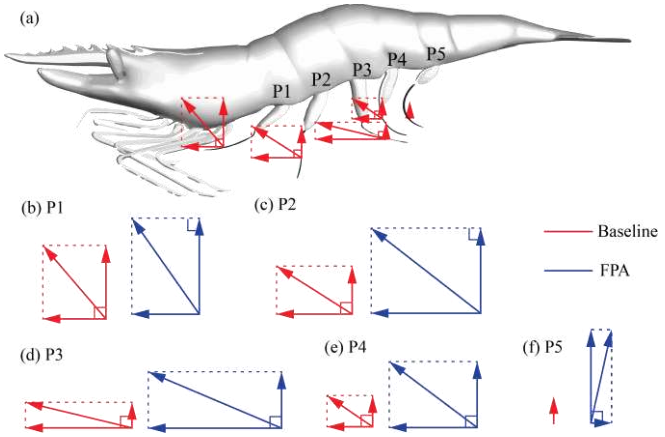

Figure 7. (a) Cycle-averaged total hydrodynamic force acting on each pleopods. (b-f) Comparison of force vector between baseline and FPA case for P1- P5.

Additionally, a comparison of the total hydrodynamic force direction on the pleopods is conducted between the baseline case and the FPA case. Figure 7a depicts the cycle-averaged total

hydrodynamic force acting on each pair of pleopods. Upon analyzing the force vectors between the two cases (Figure 7b-f), it is observed that both thrust and lift forces increase by a similar magnitude. Consequently, the direction of the total force in both cases does not exhibit significant difference. Hence, the effect of spread-out morphing motion does not alter the direction of hydrodynamic force, and consequently, the swimming direction remains unchanged.

4. CONCLUSIONS

In this study, an in-house CFD solver is employed to evaluate the effects of spread-out morphing motion of shrimp pleopods during power stroke in a forward swimming. A comparison was made with a model where the pleopod area remained fixed at its maximum. Our findings reveal that the model incorporating spread-out motion can achieve a notable reduction of 49.84% in cycle-averaged hydrodynamic power while sacrificing only 23% of cycle-averaged thrust when compared to the fixed-pleopod area model. Furthermore, the observed effect of spread-out motion leads to a 41.72% decrease in the cost of transportation by reducing body drag by 12%. This effect on thrust production mirrors its impact on lift, indicating a limited influence on the overall force direction. Additionally, our analysis highlights the presence of a high-speed zone behind the second pleopod during stroke motion, particularly near the tangent plane of the lowest tip trajectory, and a low-speed zone in front of that pleopods. Comparatively, the absence of spread-out motion results in a wider low-speed zone in front of the second pleopod.

5. ACKNOWLEDGMENTS

This work was supported by the National Science Foundation to C. Li (CBET-2451990), monitored by Dr. R. D. Joslin, and the Brown University Office of the Vice President for Research awarded to M. Wilhelmus (OVPR SEED-GR300268).

REFERENCES

1. Chateau S, Favier J, Poncet S, D'Ortona U. 2019 Why antiplectic metachronal cilia waves are optimal to transport bronchial mucus. *Phys Rev E* **100**, 042405. (doi:10.1103/PhysRevE.100.042405)

2. Ghorbani A, Najafi A. 2017 Symplectic and antiplectic waves in an array of beating cilia attached to a closed body. *Phys Rev E* **95**, 052412. (doi:10.1103/PhysRevE.95.052412)

3. Ford MP, Santhanakrishnan A. 2021 On the role of phase lag in multi-appendage metachronal swimming of euphausiids. *Bioinspir Biomim* **16**, 066007. (doi:10.1088/1748-3190/ABC930)

4. Ford MP, Lai HK, Samaee M, Santhanakrishnan A. 2019 Hydrodynamics of metachronal paddling: Effects of varying Reynolds number and phase lag. *R Soc Open Sci* **6**. (doi:10.1098/rsos.191387)

5. Sleigh M, Barlow D, Elder H, Trueman E. 1980 Metachronism and control of locomotion in animals with many propulsive structures. *Aspects of animal movement* , 49–67.

6. Lei M, Lou Z, Wang J, Dong H, Li C. 2024 Hydrodynamics of Metachronal Rowing at Intermediate Reynolds Numbers. *ASME International Mechanical Engineering Congress and Exposition, Proceedings (IMECE)* **9**. (doi:10.1115/IMECE2023-112572)

7. Byron ML *et al.* 2021 Metachronal motion across scales: current challenges and future directions. *Integr Comp Biol* **61**, 1674–1688. (doi:10.1093/icb/icab105)

8. Lionetti S *et al.* 2023 A new propulsion enhancement mechanism in metachronal rowing at intermediate Reynolds numbers. *J Fluid Mech* **974**, A45. (doi:10.1017/JFM.2023.739)

9. Colin SP, Costello JH, Sutherland KR, Gemmell BJ, Dabiri JO, Du Clos KT. 2020 The role of suction thrust in the metachronal paddles of swimming invertebrates. *Sci Rep* **10**, 1–8. (doi:10.1038/s41598-020-74745-y)

10. Daniels J, Aoki N, Havassy J, Katija K, Osborn KJ. 2021 Metachronal swimming with flexible legs: a kinematics analysis of the midwater polychaete Tomopteris. *Integr Comp Biol* **61**, 1658–1673. (doi:10.1093/ICB/ICAB059)

11. Mageean Brown, Sara Oliveira Santos, Nils B Tack, Monica M Wilhelmus. 2023 Analysis of shrimp appendage cupping on swimming performance through a bio-inspired model. In *76th Annual Meeting of the Division of Fluid Dynamics*,

12. Morris MJ, Gust G, Torres JJ. 1985 Propulsion efficiency and cost of transport for copepods: a hydromechanical model of crustacean swimming. *Mar Biol* **86**, 283–295. (doi:10.1007/BF00397515/METRICS)

13. Fish FE. 1995 Kinematics of Ducklings Swimming in Formation: Consequences of Position. *J Exp Zool*. **273**.

14. Johansson LC, Lauder G V. 2004 Hydrodynamics of surface swimming in leopard frogs (Rana pipiens). *Journal of Experimental Biology* **207**, 3945–3958. (doi:10.1242/JEB.01258)

15. Kohlhage K, Yager J. 1994 An analysis of swimming in remipede crustaceans. *Philos Trans R Soc Lond B Biol Sci* **346**, 213–221. (doi:10.1098/rstb.1994.0142)

16. Lamont EI, Emlet RB. 2018 Permanently fused setules create unusual folding fans used for swimming in cyprid larvae of barnacles. *Biological Bulletin* **235**, 185–194. (doi:10.1086/700084/VIDEO1.MP4)

17. Murphy DW, Webster DR, Kawaguchi S, King R, Yen J. 2011 Metachronal swimming in Antarctic krill: Gait kinematics and system design. *Mar Biol* **158**, 2541–2554. (doi:10.1007/s00227-011-1755-y)

18. Garayev K, Murphy DW. 2021 Metachronal swimming of mantis shrimp: kinematics and interpleopod vortex interactions. *Integr Comp Biol* **61**, 1631–1643. (doi:10.1093/icb/icab052)

19. Herrera-Amaya A, Seber EK, Murphy DW, Patry WL, Knowles TS, Bubel MM, Maas AE, Byron ML. 2021 Spatiotemporal asymmetry in metachronal rowing at intermediate Reynolds numbers. *Integr Comp Biol* **61**, 1579–1593. (doi:10.1093/icb/icab179)

20. Li C, Dong H. 2016 Three-dimensional wake topology and propulsive performance of low-aspect-ratio pitching-rolling plates. *Physics of Fluids* **28**. (doi:10.1063/1.4954505)

21. Li C, Dong H, Zhao K. 2018 A balance between aerodynamic and olfactory performance during flight in Drosophila. *Nat Commun* **9**, 1–8. (doi:10.1038/s41467-018-05708-1)

22. Lei M, Li C. 2023 Wings and whiffs: Understanding the role of aerodynamics in odor-guided flapping flight. *Physics of Fluids* **35**, 121901. (doi:10.1063/5.0174377/2925587)

23. Li C, Jiang J, Dong H, Zhao K. 2017 Computational modeling and validation of human nasal airflow under various breathing conditions. *J Biomech* **64**, 59–68.

24. Li C, Dong H. 2017 Wing kinematics measurement and aerodynamics of a dragonfly in turning flight. *Bioinspir Biomim* **12**. (doi:10.1088/1748-3190/aa5761)

25. Lei M, Li C. 2020 The aerodynamic performance of passive wing pitch in hovering flight. *Physics of Fluids* **32**. (doi:10.1063/5.0006902)

26. Liu Y, Lozano AD, Hedrick TL, Li C. 2021 Comparison of experimental and numerical studies on the flow structures of hovering hawkmoths. *J Fluids Struct* **107**, 103405. (doi:10.1016/j.jfluidstructs.2021.103405)

27. Li C. 2021 Effects of wing pitch kinematics on both aerodynamic and olfactory functions in an upwind surge. *Proc Inst Mech Eng C J Mech Eng Sci* **235**, 296–307. (doi:10.1177/0954406220907950)

28. Xu M, Wei M, Li C, Dong H. 2019 Adjoint-based optimization for thrust performance of three-dimensional pitching-rolling plate. *AIAA Journal* **57**, 3716–3727. (doi:10.2514/1.J057203)

29. Lei M, Willis MA, Schmidt BE, Li C. 2023 Numerical Investigation of Odor-Guided Navigation in Flying Insects: Impact of Turbulence, Wingbeat-Induced Flow, and Schmidt Number on Odor Plume Structures. *Biomimetics* **8**, 593. (doi:10.3390/BIOMIMETICS8080593/S1)